



# Inflow turbulence generation methods with large eddy simulation for wind effects on tall buildings



B.W. Yan, Q.S. Li\*

Dept. of Architecture and Civil Engineering, City University of Hong Kong, Kowloon, Hong Kong

## ARTICLE INFO

## Article history:

Received 30 September 2014

Received in revised form 23 February 2015

Accepted 25 April 2015

Available online 6 May 2015

## Keywords:

Inflow turbulence generation

Large eddy simulation (LES)

Tall building

Atmospheric boundary layer (ABL)

Wind loadings

## ABSTRACT

Generation of turbulent inflow conditions matching realistic wind flow characteristics in atmospheric boundary layer (ABL) is essential for accurate predictions of wind effects on buildings and structures using large eddy simulation (LES). It is thus necessary to evaluate the performances of different inflow turbulence generation techniques. In this study, four inflow turbulence generation methods (including three synthetic turbulence methods and the recycling method) were used to simulate wind flows in ABL for LES of wind loadings on a tall building. The advantages and limitations of these inflow turbulence generation methods were discussed through comparisons with available wind tunnel measurements and previous numerical simulation results. Several remedial measures were presented to improve the performances of these inflow turbulence generation methods. The findings of this paper are of use and interest to researchers and designers involved in the wind-resistant design of tall buildings, since one can follow the established procedure to predict the dynamic wind loadings on tall buildings by LES.

© 2015 Elsevier Ltd. All rights reserved.

## 1. Introduction

With the rapid development of LES techniques and the drastic increase in computing power during the last decade, LES has become a powerful tool in computational wind engineering (CWE), which has been applied to numerical simulations of the wind effects on buildings and structures [1], topographic features of complex terrain [2], pollutant dispersion in urban environment [3] and so on. For the applications of LES in CWE, an important issue that affects the numerical accuracy is to generate appropriate inflow boundary conditions with limited information from experiments or field measurements [4]. If the specifications of the mean wind speed profiles and turbulence quantities are not proper, errors exist in fluctuating pressures on building surfaces; even the most basic flow physics are probably missing [5]. To overcome this difficulty, several inflow turbulence generation techniques have been developed for LES. Keating et al. [6], Tabor and Baha-Ahmadi [7], and Huang et al. [8] have comprehensively reviewed these techniques which can be classified into three major categories: synthetic turbulence methods, precursor dataset and recycling method [6].

For the synthetic methods, the main strategy is to superimpose the mean quantities with synthetic randomness. The random perturbations can be generated with several often-used types of methods. The first family is the spectral method. Kraichnan [9] first proposed to synthesize Fourier waves for homogeneous and isotropic turbulence. In the same spirit, Smirnov et al. [10] and Batten et al. [11] developed the spectral method to reproduce general inhomogeneous and anisotropic turbulence with a tensor scaling based on the Cholesky decomposition of the local Reynolds-stress tensor [11]. Furthermore, Huang et al. [8] modified the distribution strategy of the wave vector in Kraichnan's method and generated a spatially correlated turbulent flow field satisfying arbitrary prescribed spectrum. Within the same framework proposed by Huang et al. [8], Castro and Paz [12] included a dimensionless time scale parameter to establish the temporal correlation of the synthetic velocity fluctuations. One major advantage of the spectral method is to yield an "essentially" divergence-free turbulent flow field. Recently, Yu and Bai [13] discussed the solenoidal issue (divergence-free) in detail. They introduced a vector potential field into the method by Smirnov et al. [10] and generated a strictly divergence-free turbulent flow field. Another family of turbulence synthesis techniques is the digital filter method. Klein et al. [14] used the Gaussian filter to generate inflow turbulence with spatial and temporal correlations. The advantage of this method is to produce the inhomogeneous turbulence and suitable for complex inlet

\* Corresponding author.

E-mail address: [bcqli@cityu.edu.hk](mailto:bcqli@cityu.edu.hk) (Q.S. Li).

mesh. However, it may become computationally expensive if the inlet mesh is fine. Xie and Castro [15] introduced an exponential velocity correlation function rather than Gaussian one for LES of street-scale flows. Recently, they [16] modified the incompressible solver through the velocity–pressure coupling procedure to satisfy the divergence-free property. Alternative synthetic approach is based on proper orthogonal decomposition (POD) and linear stochastic estimation (LSE) with measured fluctuating velocity field from hot wire probes or stereoscopic particle image velocimetry (SPIV) [17–19]. The last family of the inflow generation methods derived from the idea that turbulence can be reproduced by a superimposition of coherent structures with given shape, length and time scales [20]. Mathey et al. [21] introduced a random two-dimensional vortex method to superpose Gaussian-shaped streamwise vortices on the specified mean velocity profile. Then, Jarrin et al. [22] further extended the method to arbitrary-shaped vortex. Nevertheless, the statistics of turbulence (such as the low-order moments and spectrum) are not explicitly specified in its procedure.

In order to diminish the upstream fetch as short as possible, Spalart [23] introduced the recycling method of using the periodic boundaries in the streamwise direction. Lund et al. [24] adopted the rescaling idea to specify a precise inlet profile following the prescribed shear stress and momentum thickness. Lund's method was originally developed for flat-plate boundary layer and a plane of data at several boundary layer thicknesses downstream from the inlet was scaled and reintroduced at the inlet with different similarity laws for the inner and outer layers of the velocity profiles. Liu and Pletcher [25] indicated that the improper position of the recycling and rescaling plane could result in longer recycling distance and execution time. They suggested using dynamically positioned recycling plane according to instantaneous flow properties. Nozawa and Tamura [26] further developed Lund's method to simulate turbulent boundary layer flow over a rough plate. This is similar to the common practice employed in wind tunnel tests to simulate the ABL flows. Kataoka [27] simplified Lund's rescaling method using constant boundary layer thickness and generalized similarity laws. Recently, Jiang et al. [28] applied the recycling method by Kataoka [27] to generate inflow conditions for the non-isothermal boundary layer flows. The coupling of the inflow and the recycling plane is usually referred to as pseudo-periodic or semi-periodic boundary conditions, which can be integrated into the main domain in a concurrent library generation fashion. Because the inflow condition is consistent with the solution of the Navier–Stokes equations, it is believed that the turbulent flow field could possess statistical characteristics of the realistic turbulence. However, the pre-computation of the recycling domain would demand additional computational resources and cost more execution time.

The precursor dataset is to generate a library of turbulent database by running a genuine turbulence simulation, and the dataset can be remapped into the main simulation. This method is particularly suitable for Direct Numerical Simulation (DNS) [10].

It is of utmost importance to properly impose time-dependent inlet boundary condition for accurate predictions with LES [4]. The wind effects on a standard tall building have been investigated with LES by Huang et al. [29] and Daniels et al. [30]. To generate the velocity fluctuations at the inlet, Huang et al. [29] used the method by Smirnov et al. [10] and Daniels adopted the methods by Xie and Castro [15] and Kim et al. [16]. However, to the best of the authors' knowledge, comprehensive evaluation of these methods has rarely been conducted before. This study aims to assess the performances of several turbulence generation methods for LES of wind effects on tall buildings.

In the present paper, four widely used methods, including the random flow generation method (RFG) [10], the Vortex method

(VM) [21], the discretizing and synthesizing random flow generation method (DSRFG) [8] and the recycling method [26], are adopted to generate inflow turbulence for numerical simulations of wind loadings on the Commonwealth Advisory Aeronautical Council (CAARC) tall building. In this study, the computational procedure follows the workflow as illustrated in Fig. 1. Firstly, the numerical simulations in an empty computational domain are performed to check the equilibrium state of the simulated ABL using the different turbulence generation methods. Then, the simulations of the wind effects on the CAARC tall building are conducted and the performances of the turbulence generation methods are assessed through comparisons with available experimental results.

## 2. Inflow turbulence generation methods

This section presents a brief summary of the four turbulent inflow generation methods and their implementations. All the simulations reported in this paper are conducted with the finite volume method (FVM) based CFD code (Ansys/Fluent 14.0.0).

### 2.1. RFG method

The RFG method was modified by Smirnov et al. [10] on the basis of the random flow generation technique proposed by Kraichnan [9]. In this method, fluctuating velocity components are generated from the summation of Fourier harmonics. The scaling and orthogonal transformation is adopted to satisfy the divergence-free propriety and emulate inhomogeneous and anisotropic turbulence [10]. The RFG method has already been embedded into the Fluent code and is called Spectral Synthesizer. In the Fluent code formulation, the modeled spectrum, in which the wave vector and frequencies are sampled, is expressed as follows:

$$E(k) = 16(2/\pi)^{1/2} k^4 \exp(-2k^2) \quad (1)$$

where  $k$  is wave number and the number of Fourier harmonics is fixed to 100 [31]. In addition, it is required to provide the realistic inlet profiles including mean wind velocity ( $U$ ), the turbulence

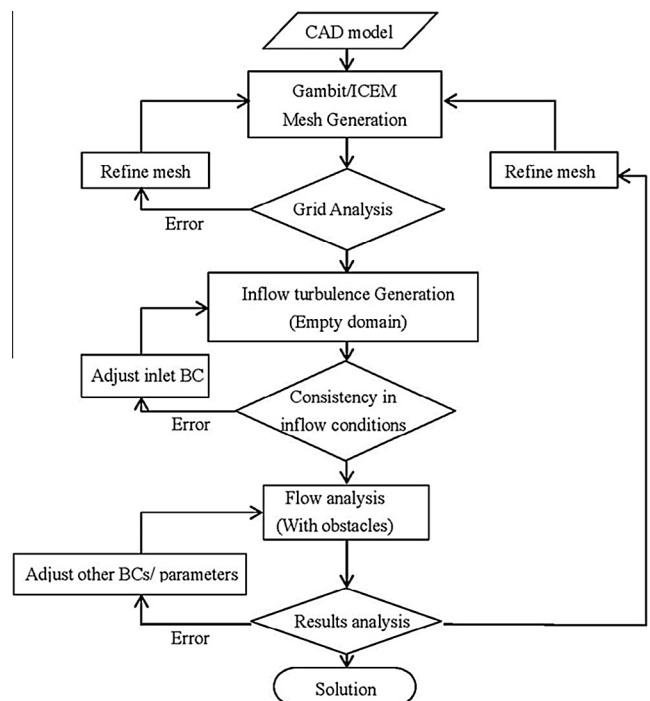


**Fig. 1.** Workflow diagram of CFD modeling in the present simulations.

kinetic energy (*TKE*) and the turbulence dissipation rate (*TDR*). It is a common practice in CWE to impose inlet profiles of *TKE* and *TDR* as follows [32]:

$$TKE = \frac{3}{2} (U \times I)^2 \quad (2)$$

$$TDR = C_{\mu}^{3/4} \frac{TKE^{3/2}}{L} \quad (3)$$

where  $C_{\mu}$  is a model constant with value of 0.09,  $U$  is the mean wind velocity,  $I$  is the turbulence intensity (TI) and  $L$  is the turbulence integral length scale (ILS). Both the turbulence intensity  $I$  and turbulence integral length scale  $L$  are specified according to the wind tunnel measurements.

## 2.2. DSRFG method

The DSRFG method was proposed by Huang et al. [8] and is capable of generating a spatially correlated turbulent flow field satisfying any target spectrum. In the present simulations, the energy spectrum of fluctuating velocity in three orthogonal directions is specified as von Karman spectrum:

$$E(k) = E(kU) = E(f) = \frac{3}{2} \frac{4(IU)^2(L/U)}{[1 + 70.8(fL/U)]^{5/6}} \quad (4)$$

where the maximum wave number is 500, the sampling number for each wave number is 100 and  $f$  is the sampled frequency. The DSRFG method was appended into the Fluent code by the authors through user define functions (UDF).

## 2.3. Vortex method (VM)

The vortex method (VM) was derived from the Lagrangian form of the two-dimensional evolution equation of the vorticity to generate turbulent inflow conditions. The fluctuating velocity field is resolved via a fluctuating two dimensional vorticity field.

The resulting discretisation for the velocity field is given as follows [21]:

$$\mathbf{u}(\mathbf{x}) = \frac{1}{2\pi} \sum_{i=1}^N \Gamma_i \frac{(\mathbf{x}_i - \mathbf{x}) \times \mathbf{z}}{|\mathbf{x}_i - \mathbf{x}|} \left( 1 - e^{-\frac{|\mathbf{x}_i - \mathbf{x}|^2}{2\sigma^2}} \right) e^{-\frac{|\mathbf{x}_i - \mathbf{x}|^2}{2\sigma^2}} \quad (5)$$

where vector  $\mathbf{z}$  is the unit vector in the streamwise direction and parameter  $\sigma$  is to control the size of a vortex. The turbulent mixing length hypothesis is used to calculate the local vortex size from the given *TKE* and *TDR* at the inlet as follows:

$$\sigma = 0.5C_{\mu}^{3/4} TKE^{3/2} / TDR \quad (6)$$

where the *TKE* and *TDR* follow Eqs. (2) and (3), respectively. It is noteworthy that a given number (here is 100) of the Gaussian-shaped vortices are superposed at the inlet and the perturbation in the streamwise direction is calculated by a simplified linear kinetic model (LKM) [21]. The VM has been incorporated into the Fluent code.

## 2.4. Recycling method

The pseudo-periodic boundary conditions are set up in the driver section. The time-averaged velocity profile at the inlet is prescribed and the velocity fluctuations are recycled between the recycling station and the inlet in the driver section as shown in Fig. 2. The velocity components at the inlet are given below:

$$\begin{aligned} u_{int}(y, z, t) &= U(z) + \phi(\theta) \times \{u(y, z, t) - U(y, z)\}_{recy} \\ v_{int}(y, z, t) &= \phi(\theta) \times \{v(y, z, t) - V(y, z)\}_{recy} \\ w_{int}(y, z, t) &= \phi(\theta) \times \{w(y, z, t) - W(y, z)\}_{recy} \end{aligned} \quad (7)$$

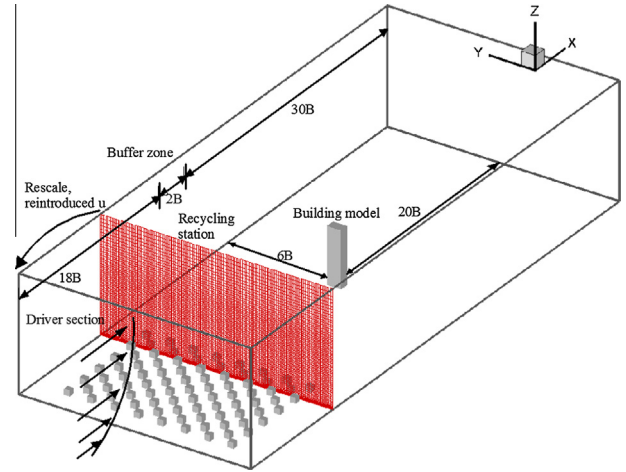


Fig. 2. Computational domain and roughness element arrangement.

where  $U, V$  and  $W$  represent the mean velocity in streamwise, spanwise and vertical directions, respectively, and  $u(y, z, t)$ ,  $v(y, z, t)$  and  $w(y, z, t)$  denote the instantaneous velocity components in these directions and the subscripts “*int*” and “*recy*” describe the quantities at the inlet and extracted from the recycling plane, respectively.  $\phi(\theta)$  is the damping function proposed by Kataoka [27] as follows:

$$\phi(\theta) = 0.5 \left\{ 1 - \frac{\tanh \left[ \frac{8.0(\theta-1.0)}{-4.0(\theta-0.3)+0.7} \right]}{\tanh(8.0)} \right\} \quad (8)$$

where  $\theta = z/\delta$ ,  $z$  is the height and  $\delta$  is the boundary layer thickness. In the Kataoka’s method, the thickness of the ABL is assumed to be constant throughout the driver section. The damping function is adopted to restrict the velocity fluctuations from developing into unstable conditions. As shown in Fig. 3, the damping ratio  $\phi(\theta)$  is highly dependent on the height from the ground and the ABL thickness. Its value becomes zero above the ABL, indicating that the velocity fluctuations outside the ABL are filtered.

In order to generate the inflow turbulence using the recycling method, it is imperative to specify the appropriate configuration of distributed roughness elements in the driver section, which can be obtained from wind tunnel experiments [25–27] or alternatively from heuristical estimates. In the present study, due to lack of this kind of information in the wind tunnel tests for the CAARC

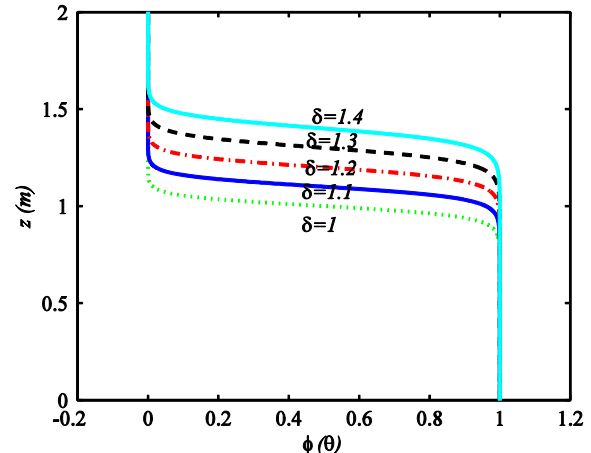


Fig. 3. Variation of the rescaling law with varying boundary thickness.

tall building, two empirical approaches for estimation of aerodynamic roughness length ( $z_0$ ) are adopted to determine the arrangements of roughness elements. Firstly, as reported by Raupach et al. [33], the parameterization of the friction velocity is associated with the roughness density  $\lambda$ , which is a function of mean frontal area of roughness elements per individual area in  $\lambda = nbh/A$  (for the total surface area  $A$  with  $n$  rectangular obstacles of width  $b$  and height  $h$ ). For the roughness density less than 0.11, a linear relation between  $\lambda$ ,  $z_0$  and  $h$  was proposed by Lettau [34] and further justified by Wooding et al. [35] as follows:

$$\frac{z_0}{h} = 0.5\lambda \quad (9)$$

where the coefficient 0.5 represents the average drag coefficient of individual obstacle.

Secondly, an empirical formula given by Engineering Science Data Unit (ESDU), which describes the variation of turbulence intensity  $I$  (TI), is given as [36]:

$$\ln\left(\frac{z}{z_0}\right) = \frac{[0.867 + 0.556 \log z - 0.246 \log^2(z)]B}{I} \quad (10)$$

where  $B$  is a parameter dependent on height  $z$ .

Two different roughness densities in the recycling method are estimated using the above two methods. The case with the roughness density  $\lambda$  of 8.6% is denoted as "R1" using the first method and the other case with the roughness density  $\lambda$  of 12.6% is named after "R2", of which the roughness length is 1.3 mm estimated by the second method. In the present simulations, the recycling method is added into the Fluent code via parallel UDF.

### 3. Computational settings and parameters

#### 3.1. Building model

The CAARC tall building model is considered herein for the comparative study. The dimensions of the rectangular prismatic building are 45.72 m ( $B$ )  $\times$  30.8 m ( $D$ )  $\times$  183.88 m ( $H$ ). This building was considered as a standard tall building and the wind loads on the building have been extensively investigated in several wind tunnels with well-documented experimental measurements [37–39].

#### 3.2. Computational domain

In the present simulation, the CAARC building is scaled down with a ratio of 1:250 which is the same as that in the wind tunnel testing by Obasaju [38]. As shown in Fig. 2, the computational domain covers 50 $B$  in the streamwise direction, 17 $B$  in the spanwise direction and 2 $H$  in the vertical direction. The blockage ratio is approximately 3%, which is regarded as acceptable in CFD.

community [40]. When using the recycling method, the auxiliary driver section with distributed roughness elements on the ground is placed in the upstream of the main computational domain. The length of the driver section is 18 $B$  as shown in Fig. 2. The velocity fluctuations are recycled and rescaled between the inlet and the recycling plane.

#### 3.3. Mesh schemes

The nesting style mesh is adopted in the main computational domain with the unstructured mesh in the neighborhood of the building and the structured mesh in the outer region as shown in Figs. 4 and 5. For the LES in Fluent, fine near-wall grid spacing ( $y^+$  in the order of unit) should be used for better results [31], where  $y^+ (\mu_t y/v)$  is the first grid wall distance normalized by the viscous length scale  $v/\mu_t$  ( $v$  is the kinetic viscosity and  $\mu_t$  is the friction velocity). The initial mesh scheme (hereinafter refer to as "baseline mesh scheme") under the  $y^+$  requirement is generated prior to the simulations based on the Schlichting skin-friction formula and the first grid wall distance to the building surfaces is specified as  $B/2000$ . In the vicinity of the tall building, the first grid spacing in the directions parallel to the wall is set as  $B/200$ , while the unstructured grid cells are generated with a growth factor of 1.05 in each direction. At the interface of the inner unstructured grid cells and external structured cells, the prismatic elements are adopted to ensure numerical stability. The advantages of the nesting grid scheme are: (1) reducing the total grid number; (2) having high grid resolution in the vicinity of the tall building. As shown in Fig. 6, the values of wall unit  $y^+$  for the baseline mesh scheme (G1) are in the order of unit based on the preliminary calculations with the standard  $k-\varepsilon$  turbulence model. Since the near-wall mesh is fine enough, the wall shear stress is obtained from the laminar stress-strain relationship. For the purpose of grid-independency check, a refined mesh scheme (G2) is generated and the grid cells around the building are refined with the coarsening factor of 2 (the refined mesh scheme divided by the baseline one). For both mesh schemes, the growth factors in the external region are 1.05 in the vertical direction and 1.1 in the transverse direction. The total grid numbers of the baseline and refined mesh schemes for the main computational domain are approximately  $2.5 \times 10^6$  (G1) and  $3.6 \times 10^6$  (G2), respectively.

For the auxiliary driver section in the recycling method, structured mesh scheme is used. To capture the wall-induced turbulence by the roughness elements and the ground, the grid points are clustered in the neighborhood of the roughness element surfaces and the ground. The first grid wall distance to the ground is around  $B/350$  and the growth factor is 1.05 in the vertical direction. The total mesh numbers of the driver sections are about  $1.3 \times 10^6$  for R1 and  $1.6 \times 10^6$  for R2, respectively.

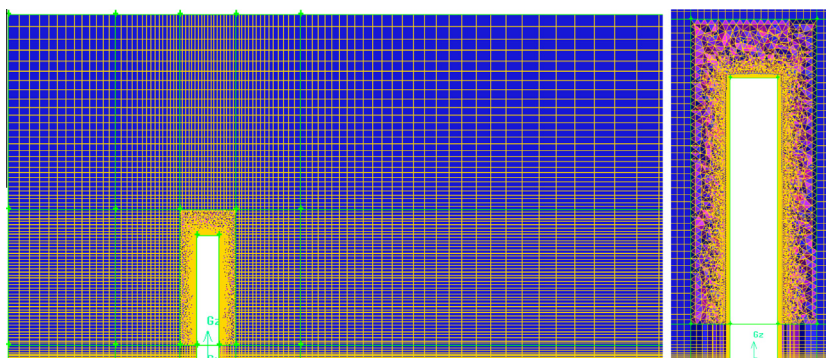
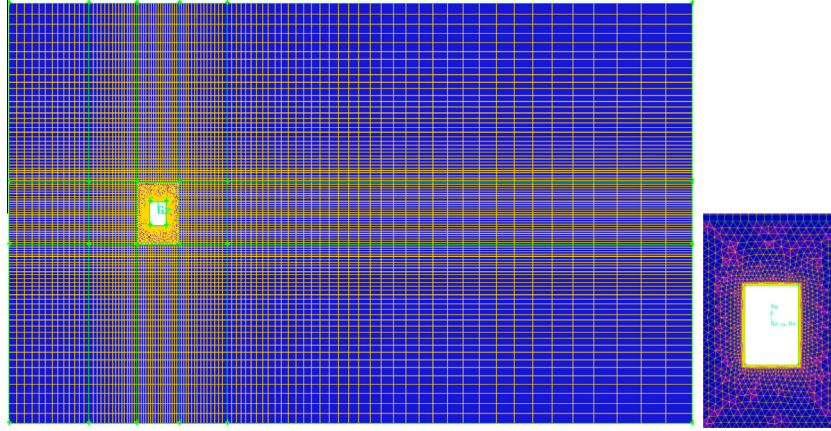


Fig. 4. Grid scheme on Y-Z plane (grid in the neighborhood of the building).



**Fig. 5.** Grid scheme on X-Y plane (grid in the neighborhood of the building).

### 3.4. Boundary conditions

At the inlet, the mean wind speed profiles with the aerodynamic roughness length ( $z_0$ ) and an exponential value of the power-law ( $\alpha$ ) are simulated. The mean wind speed profile with the aerodynamic roughness length ( $z_0$ ) follows the profile created by Obasaju in the British Maritime Technology (BMT) environmental wind tunnel as follows [38]:

$$\frac{U}{U_\tau} = 2.5 \ln \left( \frac{z - D}{z_0} \right), \quad 40 \leq \left( \frac{z - D}{z_0} \right) \leq 1000 \quad (11)$$

$$\frac{U}{U_\tau} = 2.5 \ln(40) \left( \frac{z}{40z_0 + D} \right)^{0.25}, \quad 0 \leq \left( \frac{z - D}{z_0} \right) < 40 \quad (12)$$

where  $U_\tau$  is friction velocity,  $D$  is the zero plane displacement and  $z$  is height from the ground. In the wind tunnel test,  $U_\tau = 0.92$  m/s,  $D = 10$  mm, and  $z_0 = 1.3$  mm, the mean wind speed at the building height is  $U_H = 14.5$  m/s.

The mean wind speed profile by Huang et al. [39] in the wind tunnel at Tong Ji (TJ) University follows the power law as follows:

$$\frac{U}{U_H} = \left( \frac{Z}{Z_H} \right)^\alpha \quad (13)$$

where  $U_H$  is the reference wind speed atop the building model with the value of 12.7 m/s, and  $\alpha$  is the exponential value of 0.3. For both the wind tunnel tests in BMT and TJ, the turbulence integral length scale at the building height is 0.58 m.

When using the recycling method, the streamwise pseudo-periodic boundary condition is adopted in the driver section. The distance between the recycling station and the inlet is larger than the boundary layer thickness to drive the flow over the roughness elements into fully developed conditions.

The periodic boundary conditions are used in the spanwise direction with all properties being equal at equivalent points on pairs of periodic boundaries. The symmetry boundary conditions (vanishing vertical derivatives of the streamwise and spanwise velocity components, as well as vanishing vertical velocity) are adopted at the top boundary. The zero gradient boundary conditions are set for all the variables normal to the outflow boundary. Moreover, all the surfaces of the roughness elements, the building surfaces and the ground are set as no-slip wall boundary conditions ( $u = v = 0$ ), which are appropriate for the velocity components on solid walls.

### 3.5. Subgrid-scale turbulence model

In the present simulations, the dynamic Smagorinsky-Lily model is adopted as the default subgrid-scale turbulence model, in which the model constant  $C_S$  is obtained using the dynamic procedure. In the Fluent code,  $C_S$  is fixed between zero and 0.23 to avoid numerical instability [31].

### 3.6. Solution strategy

The governing equations of incompressible flow are solved sequentially with the pressure-based segregated algorithm in Fluent code. The pressure–velocity coupling method in the present simulations is SIMPLEC (Semi-Implicit Method for Pressure-Linked Equations Consistent) algorithm [41], which is one of variants of the basic SIMPLE algorithm. The bounded central difference is used to discretize the convective and diffusion terms of the momentum equations for its relatively low diffusivity. The time derivative is discretized using the second-order backward differences and fully implicit scheme is adopted for time integration. The spatial discretization is treated implicitly. The Green-Gauss node based method is used for numerical approximation of pressure gradients, which is appropriate for the mixed structured and unstructured mesh scheme. In order to reduce the execution time, a preceding RANS simulation with superposed random noise is performed prior to each LES case as the initial conditions.

A workstation with 32 CPUs is used in parallel for the calculations. In consideration of the accuracy of the LES and

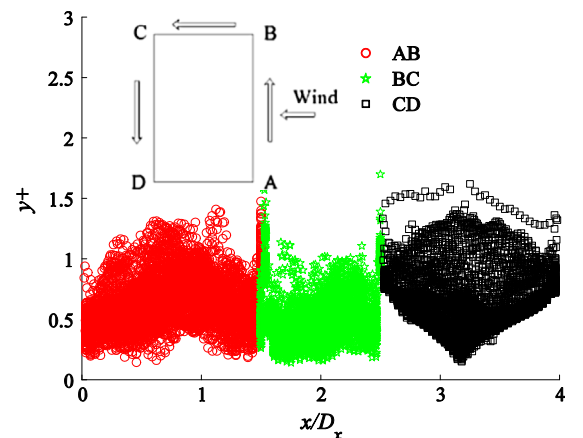


**Fig. 6.** Wall units  $y^*$  of the building surfaces for the baseline mesh G1.

computational expenses, the time step is selected to be 0.001 s and the multiple convergence criteria are utilized, in which the scaled residuals within each time step are less than  $1 \times 10^{-5}$  and the force coefficients of the building model should be within the reasonable range compared with the experimental results. A total of 20,000 time steps are calculated for each case to obtain the converged results and the statistics of the last 10,000 time steps (approximately 20 flow-through times) are sampled for flow analysis.

## 4. Results and discussions

### 4.1. Wind characteristics in an empty computational domain

It is important to simulate the equilibrium ABL profiles without longitudinal gradients [30]. To check the equilibrium state of the simulated ABL, the LES in an empty computational domain is conducted using the different turbulence generation methods prior to the numerical simulations with the building present. The time histories of velocity components in the streamwise, spanwise and vertical directions are recorded and analyzed at eleven different heights in the central region of interest.

The simulated time-averaged velocity profiles normalized by the wind speed atop the building model and the profiles of turbulence intensity are compared with the target profiles as demonstrated in Fig. 7. The mean wind speed profiles by different turbulence generators are reproduced quite well. Some discrepancies between the numerical simulations by the recycling method and the target profiles near the ground are due to shielding effects by the upstream roughness elements. For the turbulence intensity

profiles as shown in Fig. 7(c) and (d), it is evident that the turbulence levels reproduced by DSRFG and VM are closer to the experimental results, while the turbulence levels simulated by RFG and the recycling method deviate from the experimental results. As aforementioned, for the RFG method, the turbulence intensity is merely implicitly considered in the estimation of the length and time scales in Eqs. (2) and (3). So, the choice of the length scale is pretty important, while its role is not further specified [10]. Furthermore, it is worth noting that the velocity fluctuations are strongly dependent on the number of the spectral samples and it is fixed to 100 by default in the Fluent code, while that of 1000 was taken by Smirnov et al. [10]. Meanwhile, for flows over different roughness configurations (R1 and R2) in the recycling method as shown in Fig. 7(c), it can be seen that the effects of the roughness elements on the turbulence levels decrease with the height and become almost negligible above the roughness sublayer (approximately 5–6 h in the present simulations). In order to improve the turbulence levels, the quantities of TKE and TDR imposed at the inlet in the RFG method is increased iteratively following the procedure as shown in Fig. 1. In the recycling method, the weighted amplitude wave superposition (WAWS) method is used to generate the streamwise turbulence in the upper part. The WAWS equation is given below [42]:

$$u'(t) = \sqrt{2} \sum_{i=1}^N \sqrt{S_u(n_i)} \Delta n \cos(2\pi n_i t + \varphi_i) \quad (14)$$

where  $n_i$ ,  $i = 1, \dots, N$  is the sampled frequencies,  $\varphi_i$  is a uniformly distributed random phase angle between 0 and  $2\pi$ , and  $S(n_i)$  is the

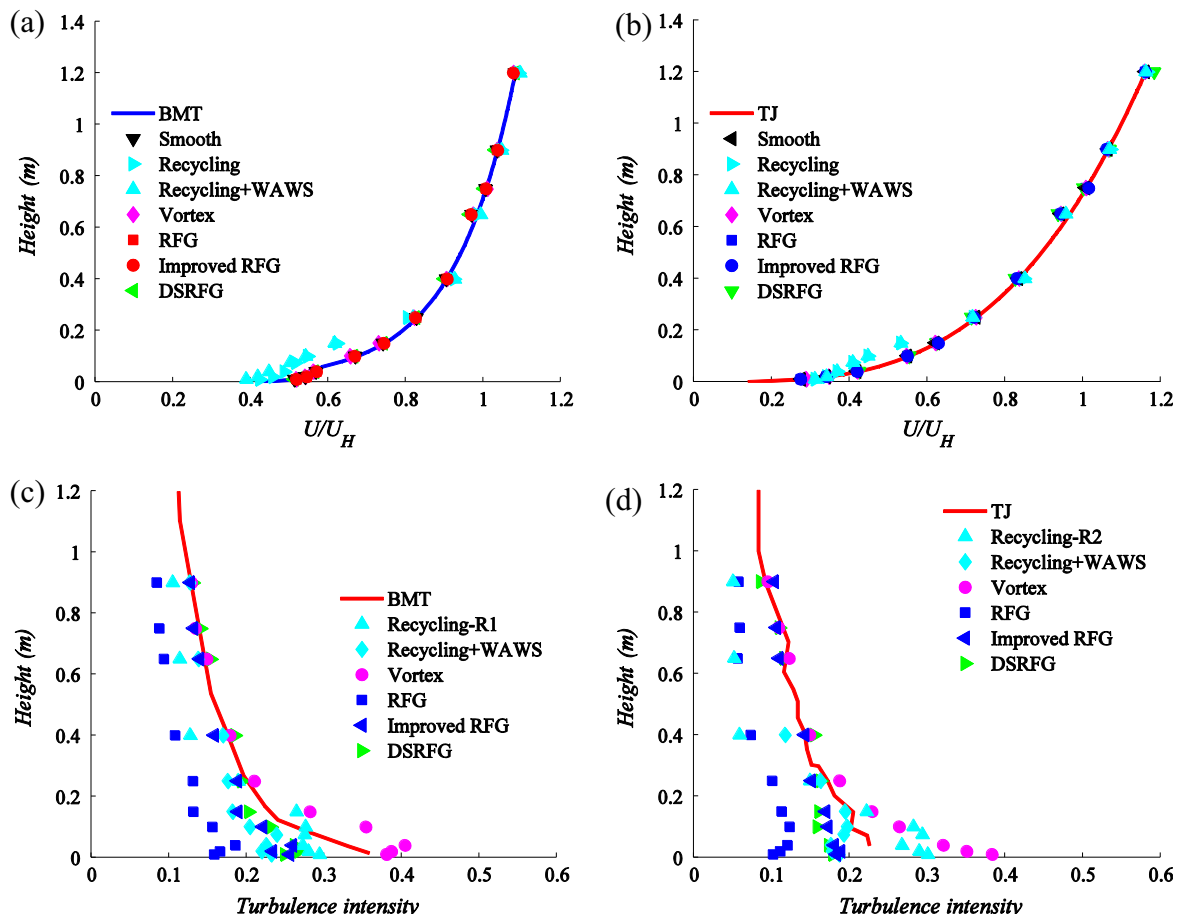


Fig. 7. Profiles of mean velocity and turbulence intensity generated in the wind tunnel tests and by the different inflow turbulence generation methods.

sampled von Karman spectrum. With the WAWS method, the additional turbulence levels are imposed at the inlet as follows:

$$I_{add} = I_{targ} - \frac{U'_{recy}(t) - U_{recy}}{U_{recy}} \quad (15)$$

where the subscripts “add” and “targ” stand for the additional and target turbulence intensity, respectively. As shown in Fig. 7(c) and (d), the improved RFG method and the recycling method with WAWS enhance the turbulence levels to a satisfactory extent.

Fig. 8 shows the normalized power spectral densities (PSD) calculated by Welch estimator from the time-histories of velocity components at the building height. Since the eddies in the inertial sub-range can be resolved by LES, it is essential to generate the fluctuating velocity satisfying the von Karman spectral model for accurate predictions of wind effects on building and structures. The velocity spectrum by DSRFG follows the von Karman spectrum quite well over a wide frequency range. The spectrum generated by VM is featured with a decay ratio of approximately  $-5/3$ , which is consistent with the previous results [21]. However, it underestimates the energy in the energy-containing subrange, which

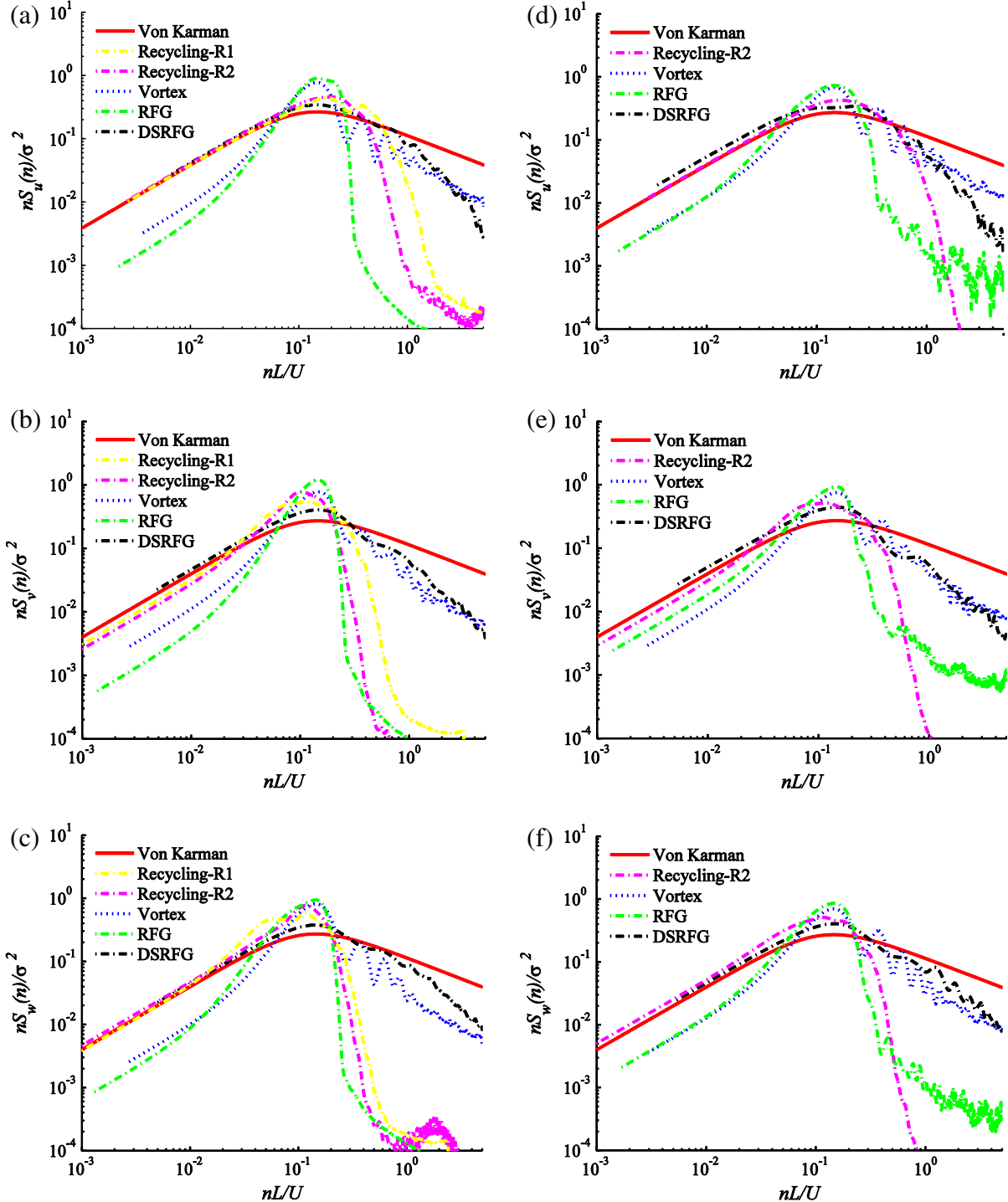


Fig. 8. Normalized power spectral densities (PSD) of  $u$ ,  $v$  and  $w$ : a.  $u$  (BMT), b.  $v$  (BMT), c.  $w$  (BMT), d.  $u$  (TJ), e.  $v$  (TJ), f.  $w$  (TJ).

**Table 1**

Comparison of turbulence integral length scale (m).

Inflow	RFG	VM	DSRFG	Recycling	Experiment
BMT	0.4378	0.7422	0.6428	0.1001 (R1)	0.58 [38]
TJ	0.4236	0.8817	0.5713	0.1613 (R2)	0.58 [39]

contains the bulk of the turbulent energy and energy production sources in the ABL [43]. The spectrum by RFG decays rapidly in the high frequency range (inertial subrange) compared to the von Karman spectrum. This is because the sampled spectrum in the RFG method is Gaussian-shaped in the Fluent code. Furthermore, the spectrum generated by the recycling method matches the von Karman spectral model quite well until the dimensionless frequency of 0.8 for R1 and 1.0 for R2 in the streamwise direction, 0.1 for R1 and 0.2 for R2 in the spanwise direction, and 0.2 for the two cases in the vertical direction. Considering the fundamental natural frequency of the CAARC building, the lower bounds of the reference wind speed atop the building can be obtained from the critical frequency ( $f_n B/U_H$ ) with the values of 25.7 m/s for R1 and 22.85 m/s for R2, which are larger than the reference wind speeds specified in the wind tunnel tests by Obasaju [38] ( $U_H = 14.5$  m/s) and Huang et al. [39] ( $U_H = 12.7$  m/s). Since the grid is generally chosen as the spatial filter in LES, only larger wave length can be resolved. It is worthy of noting in the habitant comfort analysis of tall buildings, the lower bound of the critical velocity should be smaller than the design wind speed with 1-year return period [27].

**Table 1** lists the turbulence integral length scales of the numerical simulations in comparison with the measurements in the wind tunnel tests. The length scales of the simulated flows are directly integrated from the auto-correlations of velocity fluctuations at the building height. From **Table 1**, one can see that the results by DSRFG are in good correspondence with the experimental results, while VM overestimates the length scales and the recycling method in the present simulations provides the smallest values.

#### 4.2. Wind effects on the CAARC tall building

In this section, the simulations of wind effects on the CAARC building model are conducted and compared with the available experimental results from several wind tunnel tests. For both the simulations and experiments, the windward face of the building is perpendicular to the wind flow. **Table 2** summarizes the information of the numerical and experimental cases.

**Table 2**Comparison of force coefficients between the numerical and experimental results ( $\alpha = 0^\circ$ ).

Case no.	Mesh	Inflow turbulence	Inflow	$C_D$	$C_{\sigma Fx}$	$C_L$	$C_{\sigma Fy}$
1	G1	Smooth	BMT	1.596	0.0350	0.0018	0.031
2	G2	Smooth	BMT	1.601	0.0353	0.0015	0.030
3	G1	RFG	BMT	1.8606	0.1444	-0.019	0.3317
4	G1	Improved RFG	BMT	1.8683	0.3487	0.0035	0.4257
5	G1	VM	BMT	1.9384	0.3888	0.0187	0.5151
6	G1	DSRFG	BMT	1.7594	0.3559	0.0047	0.3167
7	G2	DSRFG	BMT	1.7613	0.3497	0.0039	0.3154
8	G1	Recycling (R1)	BMT	1.6678	0.1536	0.0014	0.175
9	G1	Recycling (R1) + WAWS	BMT	1.8153	0.3375	0.0053	0.3431
10	G1	Smooth	TJ	1.6285	0.0467	0	0.041
11	G1	RFG	TJ	1.7416	0.0626	-0.0127	0.1086
12	G1	Improved RFG	TJ	1.8149	0.3176	0.0114	0.3057
13	G1	VM	TJ	1.9428	0.331	0.0144	0.4228
14	G1	DSRFG	TJ	1.8042	0.3038	0.012	0.2677
15	G1	Recycling (R2)	TJ	1.6690	0.1982	0.0187	0.1411
16	G1	Recycling (R2) + WAWS	TJ	1.7985	0.3127	0.0115	0.2437
Huang et al. [29]		RFG	TJ	1.83	0.06	0.006	0.134
Huang et al. [29]		RFG	BMT	1.90	0.118	0.004	0.3118
Experiment [38]		Turbulent	BMT	1.80	0.28	0	0.3
Experiment [38]		Uniform	BMT	1.50	0.04	-0.01	0.09

#### 4.2.1. Wind loads

The drag ( $C_D$ ) and lift force ( $C_L$ ) coefficients and their RMS values are listed in **Table 2**. The definitions of drag ( $C_D$ ) and lift ( $C_L$ ) coefficients are the same as those by Obasaju [38] as follows:

$$C_D = \frac{F_D}{0.5\rho B \int_0^H U(z)^2 dz}, \quad C_L = \frac{F_L}{0.5\rho B \int_0^H U(z)^2 dz} \quad (16)$$

where  $\rho$  is the air density,  $U(z)$  is the mean wind speed corresponding to the height  $z$ , and  $F_D$  and  $F_L$  are the steady forces acting parallel and transverse to the streamwise direction, respectively. In order to account for the mean wind speed profile,  $\int_0^H U(z)^2 dz$  is considered herein. Substituting the mean wind speed profile expressed in Eq. (11) into the integration, one has:

$$\int_0^H U(z)^2 dz \approx 0.7315 U_H^2 H \quad (17)$$

For the mean wind speed profile defined in Eq. (13), we have:

$$\int_0^H U(z)^2 dz = 0.625 U_H^2 H \quad (18)$$

The RMS values of  $F_D$  and  $F_L$  are denoted by  $\sigma_{FD}$  and  $\sigma_{FL}$ , and the corresponding coefficients are defined below:

$$C_{\sigma Fx} = \frac{\sigma_{Fx}}{0.5\rho U_H^2 BH}, \quad C_{\sigma Fy} = \frac{\sigma_{Fy}}{0.5\rho U_H^2 BH} \quad (19)$$

From the comparisons between the present and previous simulations [29] and the wind tunnel experimental results [38] as listed in **Table 2**, it can be found that:

- (1) The cases for the CAARC building immersed in smooth flows (case 1 and case 2) under-predict  $C_L$  and  $C_D$  compared with the wind tunnel measurements. The drag force coefficient  $C_D$  is underestimated by about 12%. The RMS values  $C_{\sigma FD}$  and  $C_{\sigma FL}$  are almost zero, which shows that the fluctuating forces on the building model are not reproduced well in the smooth flows. In addition, case 1 (smooth flow) seems to yield the value of  $C_D$  close to the experimental result in uniform flow by Obasaju [38]. However, it is noteworthy that the wind shear profile was adopted in case 1, while uniform velocity was used in the wind tunnel test by Obasaju and the boundary layer thickness was only 150 mm [38]. By contrast, the RFG and DSRFG methods provide satisfactory predictions of  $C_D$  with discrepancies less than 3.5%,

while VM overestimates  $C_D$  by 7.2% and the recycling method with R1 underestimates  $C_D$  by 7.8%. The simulations with DSRFG, VM, improved RFG and the recycling method with WAWS give reasonable fluctuating force coefficients compared with the experimental results. From the above comparisons, one can find that the inflow turbulence generators can improve the predictions of both the mean and fluctuating force coefficients.

- (2) Grid independence check is performed between case 1 and case 2 in the smooth flows and between case 6 and case 7 in turbulent flows. The differences of the results obtained from the two different mesh schemes are quite small, indicating that the baseline mesh scheme G1 is fine enough, although a slight improvement is observed with the mesh refinement.

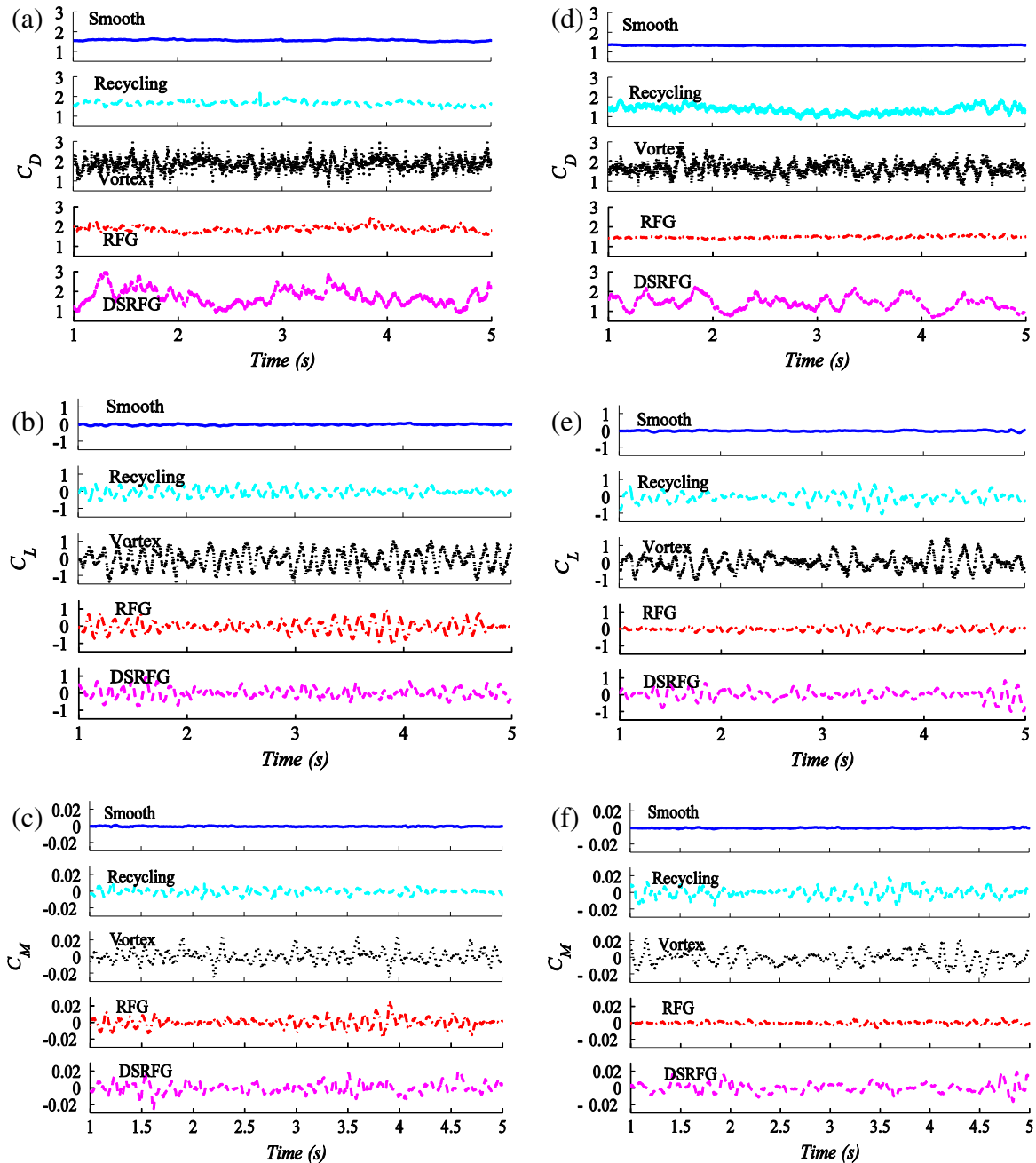
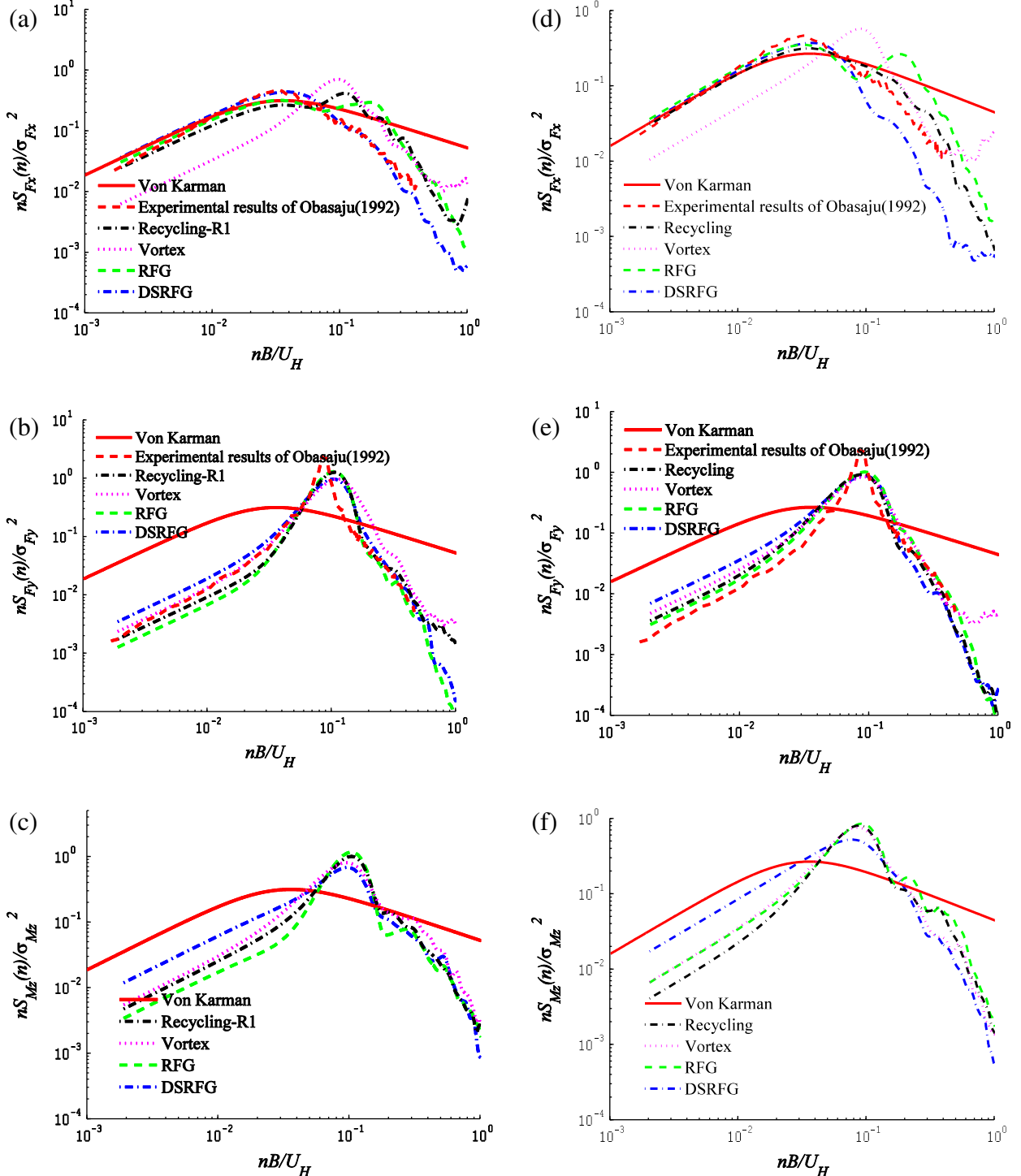


Fig. 9. Time histories of  $C_D$ ,  $C_L$  and  $C_M$  under the BMT (a–c) and TJ (d–f) inflow conditions.

Fig. 9 illustrates time-histories of the force coefficients  $C_D$ ,  $C_L$  and  $C_M$  under the BMT and TJ inflow conditions using the different turbulent inflow generation methods. It can be seen that all the lift and moment coefficients with the inflow turbulence generation methods vary in a regular and periodic pattern, which is associated with the existence of vortex shedding. The time history of the drag force coefficient  $C_D$  by VM is much more regular and possesses the pseudo-vortex behavior, since the streamwise velocity perturbation in VM is generated by imitating the planar vortex.

Fig. 10 shows the normalized PSDs of along-wind force  $F_x$ , across-wind force  $F_y$  and torsional moment  $M_z$  from the numerical simulations with the different inflow turbulence generators. The PSDs of  $F_x$  and  $F_y$  obtained from the Obasaju's measurements [38] and the von Karman spectral model are also demonstrated for comparison purposes. It can be observed that:



**Fig. 10.** Spectra of along-wind force, across-wind force and torsional moment under the BMT inflow conditions (a–c) and the TJ inflow conditions (d–f).

- The spectra of  $F_x$  predicted by DSRFG, RFG and the recycling method are generally similar, while DSRFG provides better agreement with the experimental measurements. The force spectral peak is located at the reduced frequency of about 0.03. Meanwhile, the reduced frequency of the spectral peak by VM is evident about 0.1, which is larger than those by the other methods and coincides the spectral peak of the across-wind force  $F_y$ . As discussed above, VM provides the periodically varying along-wind force and the sharp peak of the along-wind force spectrum is associated with the

well-organized vortex shedding. This indicates that  $F_x$  obtained by VM possesses the similar vortex-induced mechanism as that in the across-wind force. Therefore, the energy distribution by VM is distorted in the along-wind direction. As shown in Fig. 10(a) and (d), another local peak in the spectra by DSRFG, the recycling method and VM is observed in the reduced frequency range of 2–3 Hz. This may be due to the fact that the large-scale vortices are drastically smashed into small scales with the increase of the vortex movement, which is also justified by the instantaneous flow field shown in Fig. 11.

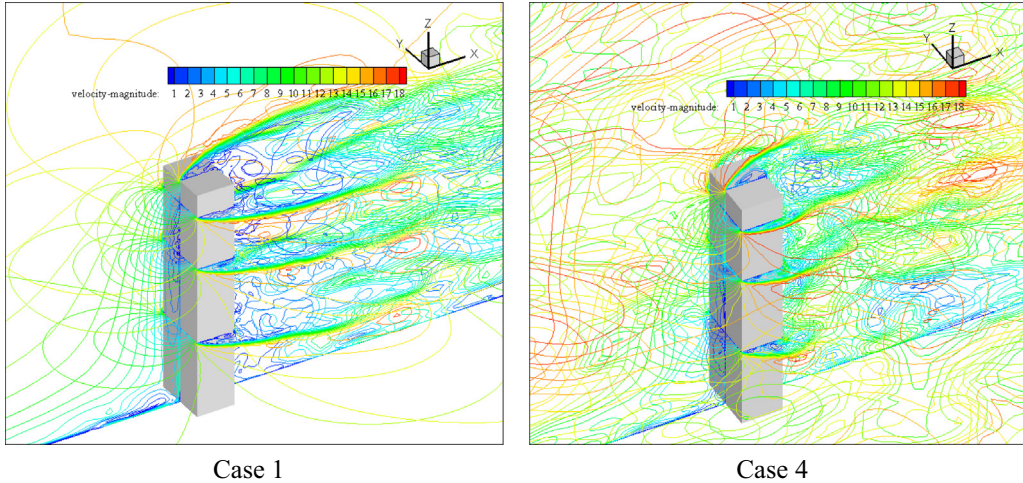


**Fig. 11.** Instantaneous velocity contours with streamlines on planes at  $y = 0$ ,  $z = 1/3H$ ,  $z = 2/3H$ ,  $z = 9/10H$  of Case 1 (in smooth flow) and Case 4 (in turbulent flow).

- (2) Sharp peaks occur in the spectra of  $F_y$  in all the simulations and the experimental results. These turbulent inflow generation methods well reproduce the spectral peaks at the reduced frequency of about 0.11, which is associated with the vortex shedding and quite close to the Strouhal number  $S$  ( $S = nb/U$ ) of 0.12 for a square cylinder.
- (3) For  $M_z$ , the spectra show the similar pattern as that of the spectra of  $F_y$  and the sharp spectral peak occurs at the reduced frequency of 0.11. Due to the bulk of vortices generated near the lateral sides and in the wake region, the unsteady pressure distributions on the lateral surfaces of the buildings model are uneven, which intensifies the torsional moments of the tall building. For this reason, the wind-induced torsional moment is predominately coupled with the shedding vortex and shares the same mechanism as the across-wind force.

To further verify the accuracy of the simulations, pressure coefficients  $C_p$  are compared with the experimental results from several wind tunnel studies. The pressure coefficient  $C_p$  is defined below:

$$C_p = 2(P - P_0)/(\rho U_H^2) \quad (20)$$

where  $P$  is dynamic pressure and  $P_0$  is the reference pressure with a value of 1 atm and specified atop the building model in the present numerical simulations.

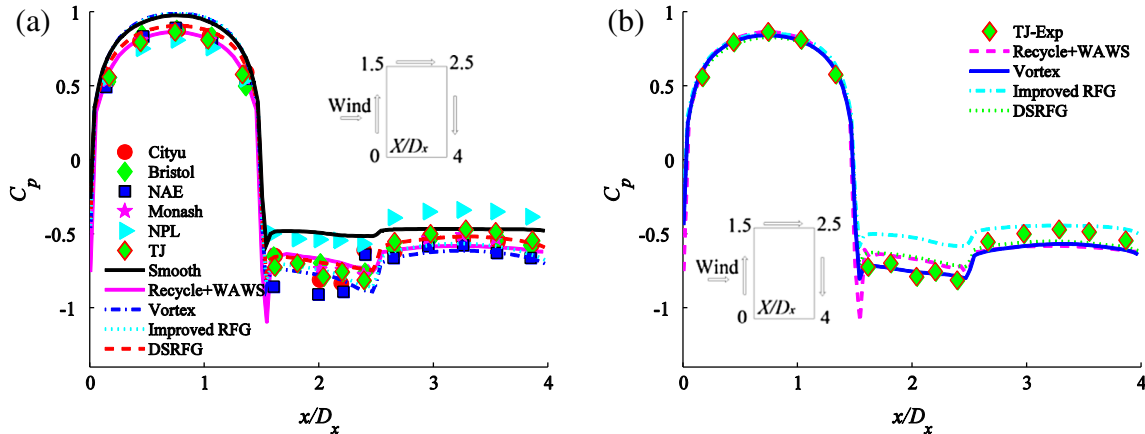


**Fig. 12.** Mean pressure coefficients at  $2/3H$  under the BMT inflow conditions (a) and TJ inflow conditions (b).

Due to lack of the pressure measurement results in the wind tunnel study conducted by Obasaju [38], the pressure coefficients measured at other wind tunnel labs [37] are collected for comparison herein. These labs are at the City University, England; Monash University, Australia; National Aeronautical Establishment (NAE), Canada; National Physical Laboratory (NPL), England; Bristol University, England. Meanwhile, the results of the surface pressures on the building model measured by Huang et al. [39] at Tongji University, China are also considered herein. The correction to the blockage effect was not performed to the pressure data due to lack of reliable methods.

Fig. 12 shows the comparison of the mean pressure coefficients  $C_p$  at  $2/3H$  between the numerical results and the experimental measurements. The calculated results match the experimental data fairly well in general, although some slight discrepancies still exist.

On the windward surface of the building model, the overall performances of the numerical simulations are quite satisfactory, while the cases in the smooth flows and by VM slightly overestimate the mean pressure coefficients. As shown in Fig. 12(b), the numerical results are consistent with the experimental measurements by Huang et al. [39]. Although the experimental measurements as shown in Fig. 12(a) were collected from various wind tunnel laboratories with different Reynolds numbers, blockage ratios and inflow boundary conditions, etc., the mean pressure coefficients on the front surface show quite little difference among them.

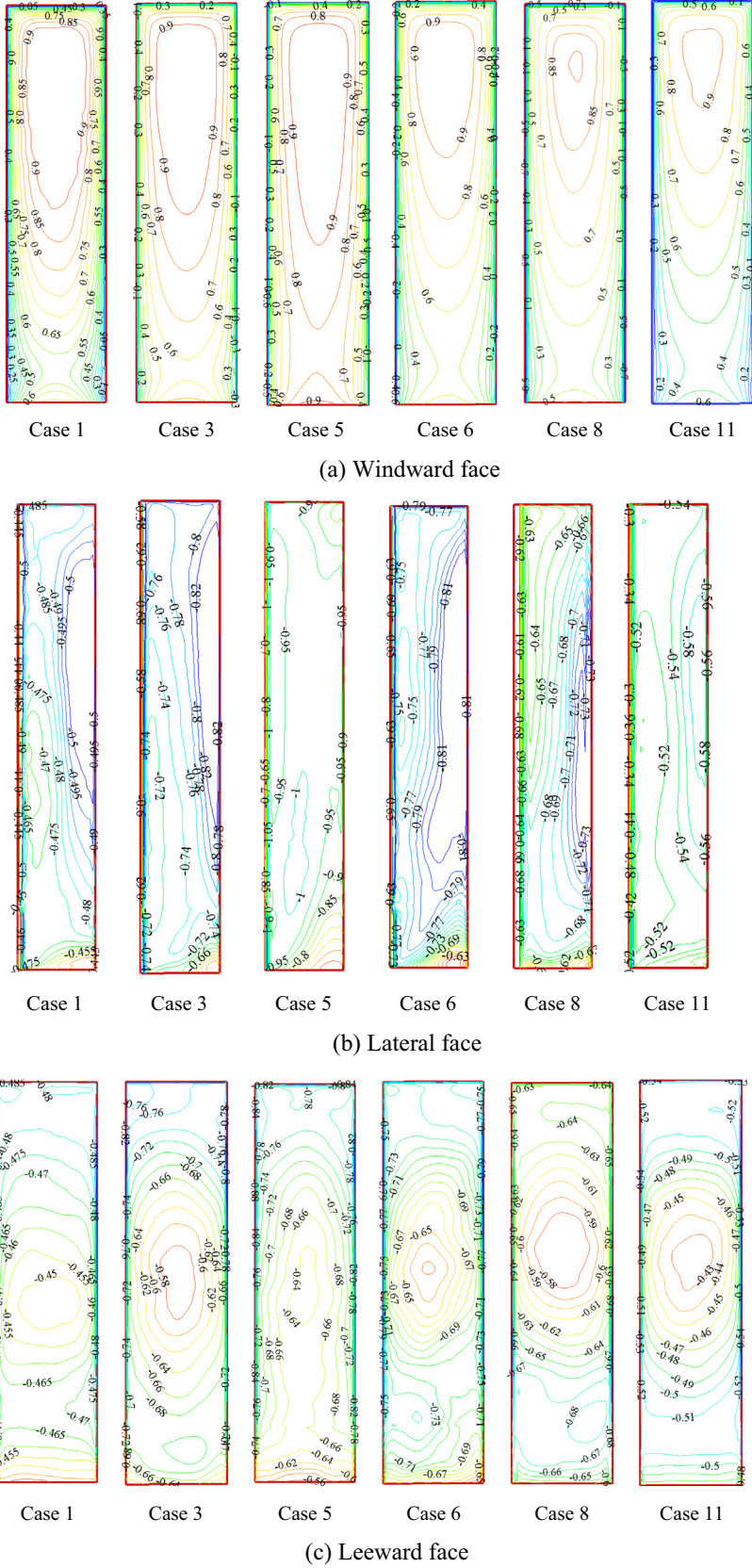


Fig. 13. Mean pressure coefficient contours.

On the lateral and leeward faces, the mean pressure coefficients by the numerical simulations are comparable with each other and enveloped by the experimental results. However, the differences in

the magnitude are noticeable, implying that the mean pressure coefficients on the lateral and leeward faces are sensitive to the inflow boundary conditions generated by the different turbulence

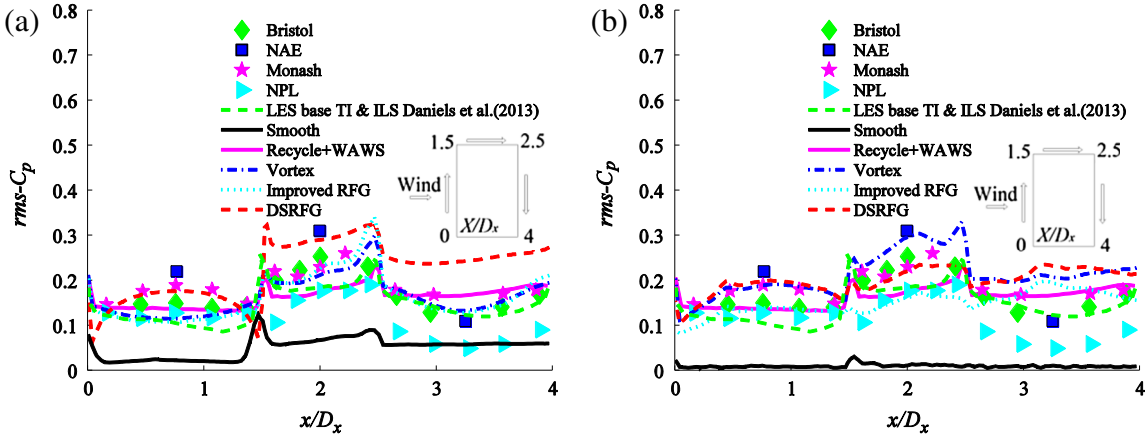


Fig. 14. RMS pressure coefficients at  $2/3H$  under the BMT inflow conditions (a) and TJ inflow conditions (b).

generation methods. This is due to the fact that turbulence characteristics of approaching flows could have significant effects on the (mean, RMS and peak) pressure coefficients [44]. However, as shown in Fig. 12(a), all the numerical results fall in the range of the scattered experimental data except for the cases in the smooth flows. Moreover, as shown in Fig. 12(b), under the TJ inflow condition, DSRFG and VM give better predictions.

Fig. 13 shows the pressure contours of different numerical simulations. Unlike the similar mean pressure coefficient distributions on the windward face, substantial discrepancies of the mean pressure coefficient contours on the lateral and leeward faces are observed. Obasaju [38] indicated that high local base suction associated with organized vortex shedding might arise near the bottom of the leeward face, and the local high negative pressure coefficients are discerned in Fig. 13(c). On the lateral faces, in the vicinity of the frontal sharp corner, VM gives higher negative pressure coefficients, while the contour patterns and magnitudes by RFG, VM and the recycling method are fairly similar.

The numerical RMS pressure coefficients are presented in Fig. 14 in comparison with the wind tunnel experimental data and the previous simulation results [30]. The RMS pressure coefficient contours are shown in Fig. 15. It is apparent that:

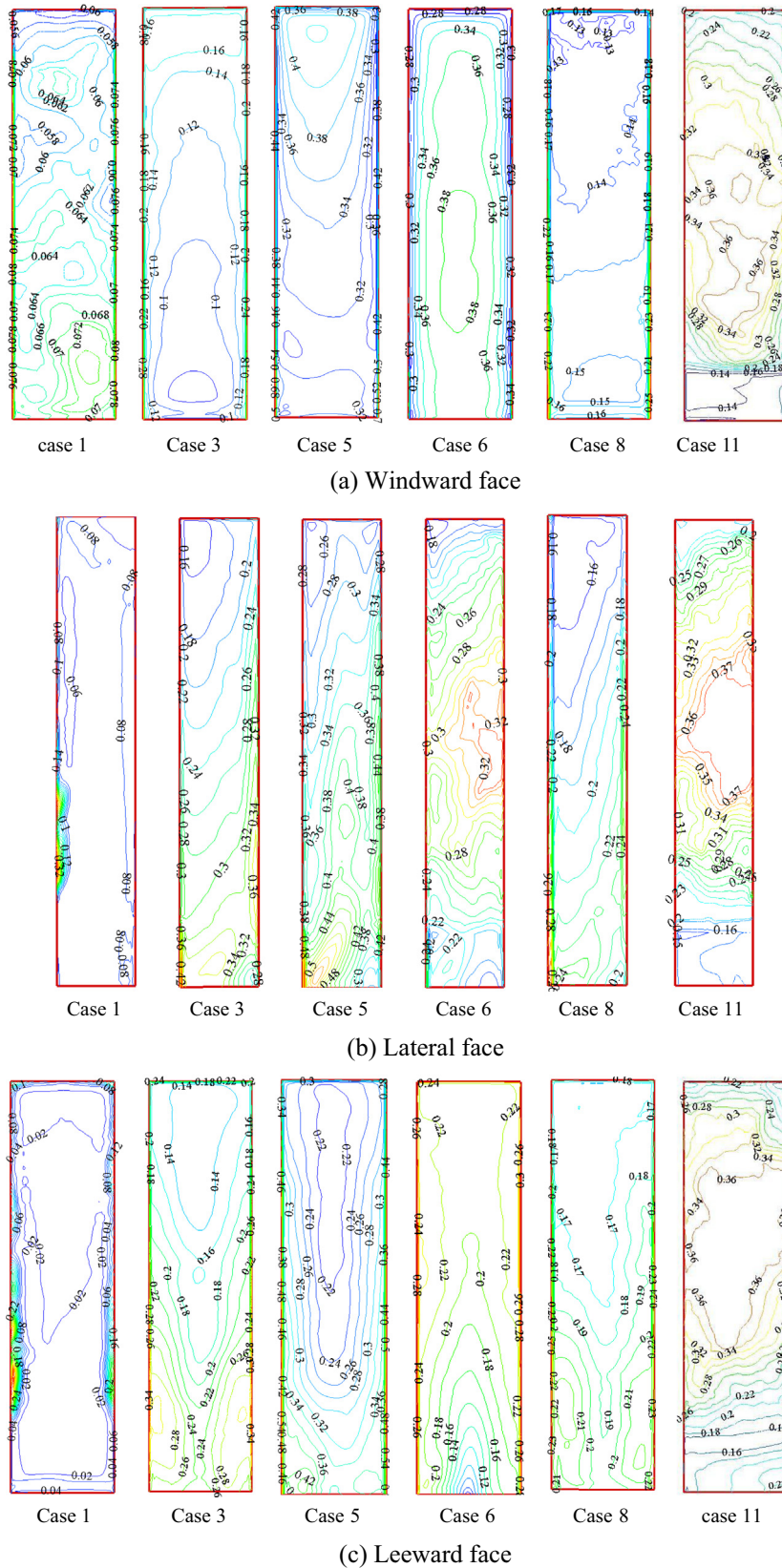
- (1) The RMS pressure coefficients collected from the different wind tunnel studies are divergent over the range of 0.1–0.3 due to the differences of turbulence intensities generated in the wind tunnel tests [45]. The numerical results are mostly wrapped by the scattered experimental data, while DSRFG and VM provide slight overestimations on the leeward face. As expected, the fluctuating pressure coefficients in the smooth flows are quite trivial. This confirms the importance and necessity of appropriate superposition of inflow turbulence at the inlet when using LES.
- (2) The RMS pressure coefficient contours are considerably different among the simulations. For those predicted by the same inflow turbulence generator but with different inflow conditions (case 3 and case 11), the contour patterns are also quite different with each other.

#### 4.2.2. Flow fields

The flow pattern around a cube immersed in uniform flow over a relatively smooth ground has been well summarized based on the detailed visualization and LDA measurement by Martinuzzi [46]. The flow pattern can be described as: (1) a horseshoe vortex forms and wraps around the cube near the ground, and also extends to the downstream; (2) the flow separates at the front

edge of the roof and side walls and develops a separation region; (3) in the lee of the obstacle, a large separation zone evolves with a strong bow vortex. Further investigation on a cube standing in the ABL (the boundary thickness is several times the height of the cube) was conducted by Davies et al. [47], and it was observed that the recirculating region in the lee of the cube was contracted and a strong base suction was speculated. This speculation was confirmed in the wind tunnel study by Obasaju [38]. As shown in Table 2, the drag coefficient  $C_D$  is increased from 1.49 to 1.80 when the inflow conditions are changed from the uniform flow to the boundary layer flow. The two dimensional mean flow patterns on the horizontal and vertical planes are shown in Figs. 16 and 17, respectively. It is observed that:

- (1) The characteristics of the flow patterns as mentioned above are well reproduced in all the cases, while some inconsistencies are also observed. The shapes and locations of the bow vortex predicted by the different inflow generation methods are pretty different. As shown in Fig. 16(a) and (f), the bow vortex location predicted in the smooth flow is extended to the most downstream and its shape is relatively flat as shown in Fig. 17(a). Moreover, the numerical results of case 5 and case 13 using VM under different inflow conditions as shown in Fig. 16(c) and (h) reveal that the bow vortex located nearest to the leeside of the building and its shape is quite oblique. This is consistent with the pressure distribution on the leeward face, since the more downstream the bow vortex is extended, the smaller the leeside negative pressure is (more recovered from the vortex movement).
- (2) For the predicted flow contraction of the recirculating region, the smooth flow results in the predictable smallest contraction degree as shown in Fig. 16(a). The recirculation region by VM is most contracted as demonstrated in Fig. 17(c) and stronger base suction is reproduced on the leeward face as illustrated in Fig. 13(c).
- (3) The separation angle near the corners of the lateral faces predicted in the smooth flow is rather smaller and the streamlines are fairly smooth within the smaller separation region near the side faces. It is also observed that the location and the shape of the bow vortex and the contraction degree of the recirculating flow region are fairly different when the simulations are performed under different inflow conditions. This also explains the discrepancies of the pressure coefficients and the drag force coefficients among different cases.

**Fig. 15.** RMS pressure coefficient contour.

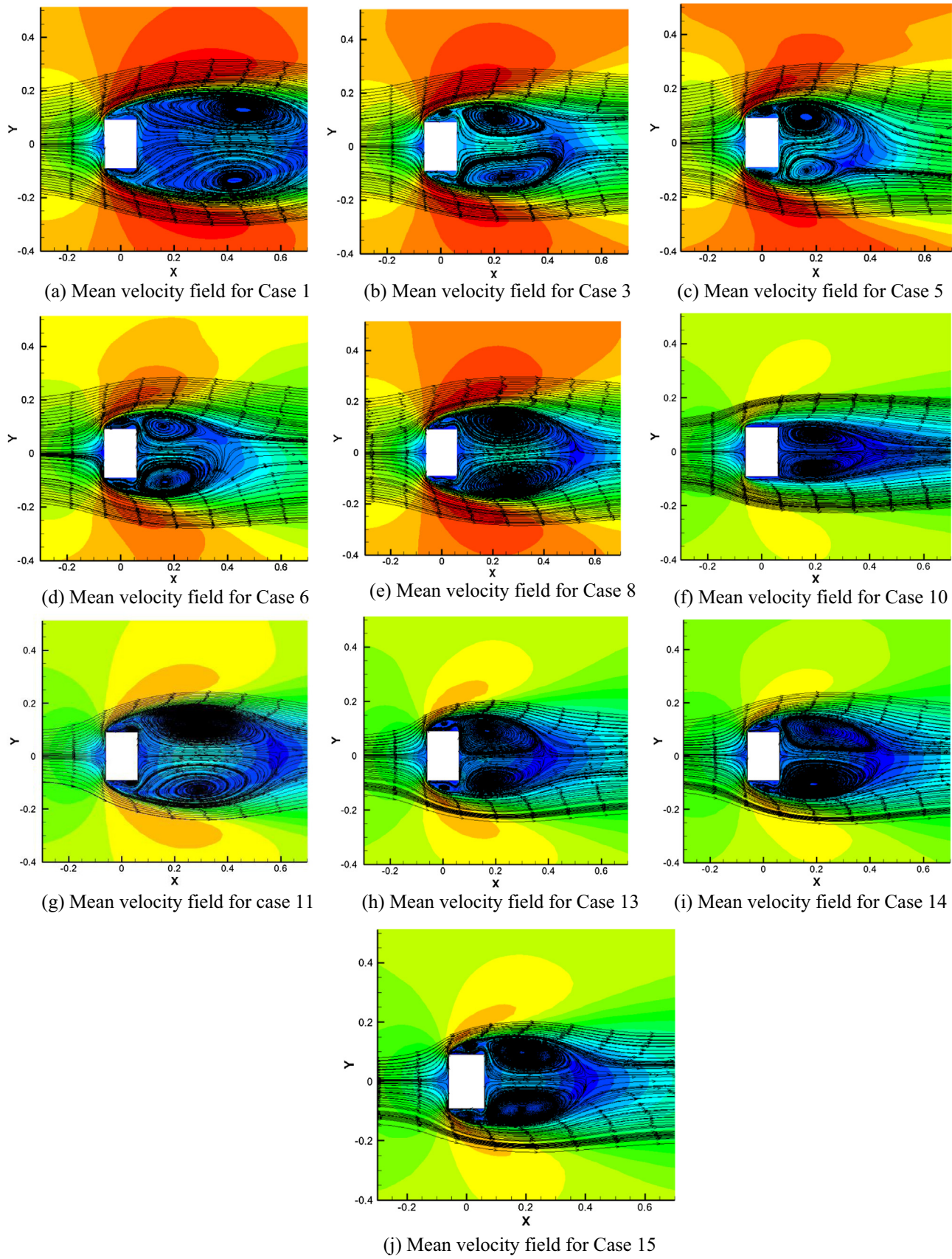


**Fig. 16.** Mean velocity contours with streamlines on X-Y plane at  $z = 2/3H$  with the BMT and TJ inflow conditions.

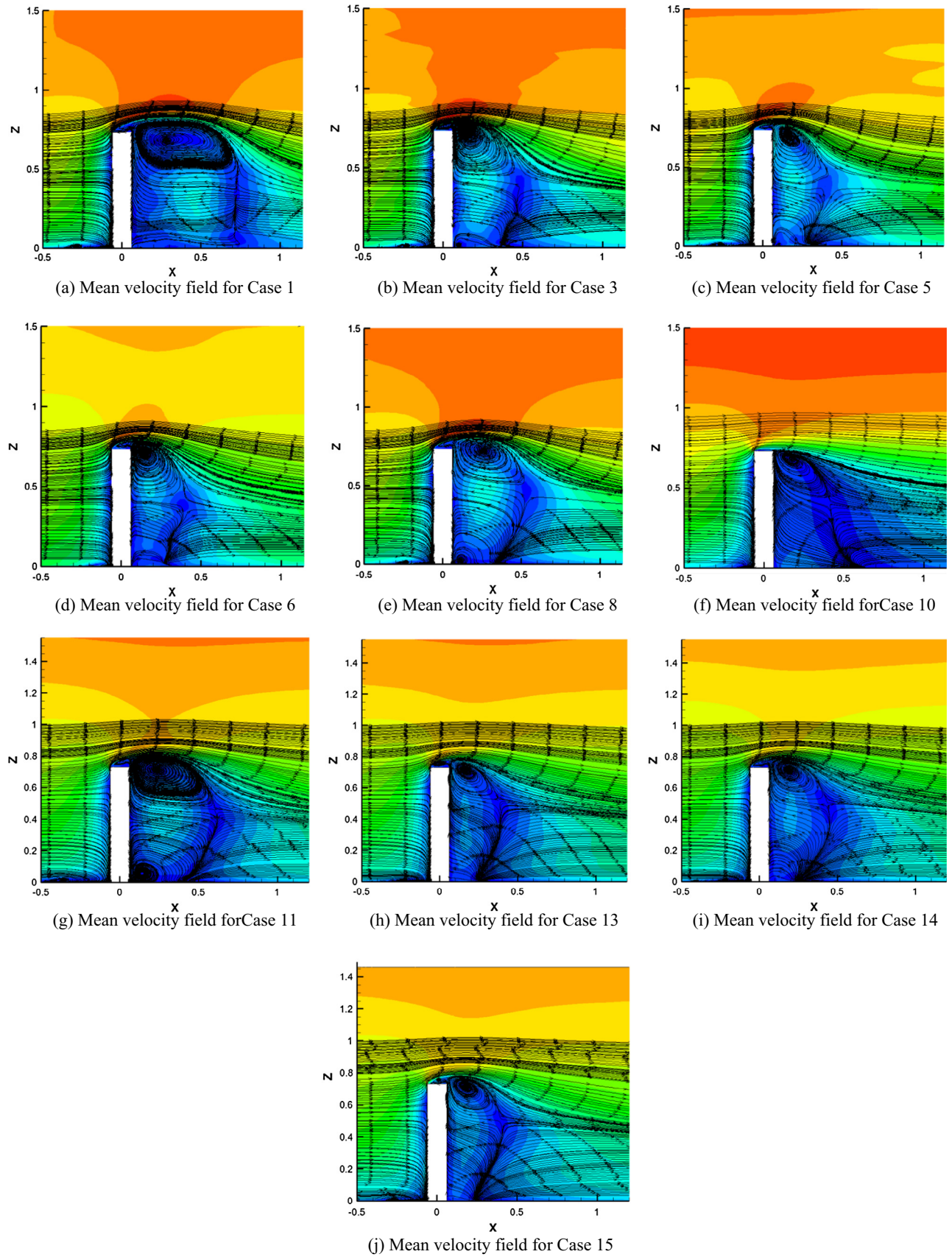


**Fig. 17.** Mean velocity contours with streamlines on  $X$ - $Z$  plane at  $y = 0$  with the BMT and TJ inflow conditions.

## 5. Conclusions

The LES for wind effects on a standard tall building model were performed based on four widely used inflow turbulence generation methods. The performances of the four methods have been assessed through comparisons with the available wind tunnel testing results. Furthermore, remedial measures were given to improve the performances of RFG and the recycling method. The results showed that the appropriate superposition of turbulent inflow is of significance for the accurate estimations of wind effects on the tall building. The main conclusions are summarized as follows:

- (1) The equilibrium state check in an empty computational domain was included in the workflow of the present CFD modeling, which is useful or essential for other similar problems.
- (2) When using the recycling method, the effects of the roughness elements upon the turbulence levels were confined in the roughness sublayer. The combined WAWS method in the upper region was able to improve the turbulence level to a satisfactory extent, although the computational cost would increase.
- (3) As far as it is concerned for the habitant comfort assessment of a tall building, two issues should be taken into account. One is that the grid resolution in the driver section for the recycling method or the subdomain between the inlet and the concerned building should be adequately fine to reproduce the high-frequency components of fluctuating velocity. The other is that an appropriate spectrum of wind flow in the ABL, such as von Karman spectral model, should be adopted as a target spectrum in the turbulence synthesis method.
- (4) Among all the four turbulence inflow generation methods, the overall performance of DSRFG was generally satisfactory and appropriate for the predictions of dynamic wind loads on tall buildings by LES.
- (5) The flow fields around the tall building were reasonably simulated in the present LES. The effects of inflow turbulence on the reproduction of complex flow phenomena such as flow separation, vortex shedding, bow vortex at the back side and horse-shoe vortex wrapped around the bluff body were investigated and discussed. Moreover, with the superposition of inflow turbulence in the LES, the contraction of the recirculating flow behind the bluff body immersed in the ABL was significantly intensified and the wind-induced suction on the leeward face of the building were greatly increased.

## Acknowledgements

The work described in this paper was fully supported by grants from the National Natural Science Foundation of China (Project No: 51178179 and 91215302) and a grant from the Research Grants Council of Hong Kong Special Administrative Region, China (Project No: CityU 118213). The authors thank the reviewers for their valuable comments and suggestions.

## References

- [1] Nozu T, Tamura T, Okuda Y, Sanada S. LES of the flow and building wall pressures in the center of Tokyo. *J Wind Eng Ind Aerodyn* 2008;96:1762–73.
- [2] Uchida T, Ohya Y. Large-eddy simulation of turbulent airflow over complex terrain. *J Wind Eng Ind Aerodyn* 2003;91:219–29.
- [3] Nozu T, Tamura T. LES of turbulent wind and gas dispersion in a city. *J Wind Eng Ind Aerodyn* 2012;104–106:492–9.
- [4] Tamura T. Towards practical use of LES in wind engineering. *J Wind Eng Ind Aerodyn* 2008;96:1451–71.
- [5] Cochran L, Derickson R. A physical modeler's view of Computational Wind Engineering. *J Wind Eng Ind Aerodyn* 2011;99:139–53.
- [6] Keating A, Piomelli U, Balaras E, Kaltenbach HJ. A priori and a posteriori tests of inflow conditions for large-eddy simulation. *Phys Fluids* 2004;16:4696–712.
- [7] Tabor GR, Baha-Ahmadi MH. Inlet conditions for large eddy simulation: a review. *Comput Fluids* 2010;39:553–67.
- [8] Huang SH, Li QS, Wu JR. A general inflow turbulence generator for large eddy simulation. *J Wind Eng Ind Aerodyn* 2010;98:600–17.
- [9] Kraichnan RH. Diffusion by a random velocity field. *Phys Fluids* 1970;13(1):22–31.
- [10] Smirnov R, Shi S, Celik I. Random flow generation technique for large eddy simulations and particle-dynamics modeling. *J Fluids Eng* 2001;123:359–71.
- [11] Batten P, Goldberg U, Chakravarthy S. Interfacing statistical turbulence closures with large-eddy simulation. *AIAA J* 2004;42:485–92.
- [12] Castro HG, Paz RR. A time and space correlated turbulence synthesis method for large eddy simulations. *J Comput Phys* 2012;235:742–63.
- [13] Yu RX, Bai XS. A fully divergence-free method for generation of inhomogeneous and anisotropic turbulence with large spatial variation. *J Comput Phys* 2014;256:234–53.
- [14] Klein M, Sadiki A, Janicka J. A digital filter based generation of inflow data for spatially developing direct numerical or large eddy simulations. *J Comput Phys* 2003;186:652–65.
- [15] Xie ZT, Castro IP. Efficient generation of inflow conditions for large eddy simulation of street-scale flow. *Flow Turbul Combust* 2008;81:449–70.
- [16] Kim Y, Castro IP, Xie ZT. Divergence-free turbulence inflow conditions for large-eddy simulations with incompressible flow solvers. *Comput Fluids* 2013;84:56–68.
- [17] Perret L, Delville J, Manceau R, Bonnet JP. Generation of turbulent inflow conditions for large eddy simulation from stereoscopic PIV measurements. *Int J Heat Fluid Flow* 2006;27:576–84.
- [18] Maruyama Y, Tamura T, Okuda Y, Ohashi M. LES of turbulent boundary layer for inflow generation using stereo PIV measurement data. *J Wind Eng Ind Aerodyn* 2012;104–106:379–88.
- [19] Maruyama Y, Tamura T, Okuda Y, Ohashi M. LES of fluctuating wind pressure on a 3D square cylinder for PIV-based inflow turbulence. *J Wind Eng Ind Aerodyn* 2013;122:130–7.
- [20] Pamiés M, Weiss PE, Garnier E, Deck S, Sagaut P. Generation of synthetic turbulent inflow data for large eddy simulation of spatially evolving wall-bounded flows. *Phys Fluids* 2009;21:045103.
- [21] Mathey F, Cokljat D, Bertoglio JP, Sergent E. Assessment of the vortex method for large eddy simulation inlet conditions. *Prog Comput Fluid Dyn* 2006;6:58–67.
- [22] Jarrin N, Benhamadouche S, Laurence D, Prosser R. A synthetic eddy method for generating inflow conditions for large-eddy simulations. *Int J Heat Fluid Flow* 2006;27:585–93.
- [23] Spalart PR. Direct numerical simulation of turbulent boundary layer up to  $Re_\theta = 1410$ . *J Fluid Mech* 1988;187:61–98.
- [24] Lund TS, Wu X, Squires KD. Generation of turbulent inflow data for spatially-developing boundary layer simulation. *J Comput Phys* 1998;140:233–58.
- [25] Liu KL, Pletcher RH. Inflow conditions for the large eddy simulation of turbulent boundary layers: a dynamic recycling procedure. *J Comput Phys* 2006;219:1–6.
- [26] Nozawa K, Tamura T. Large eddy simulation of the flow around a low-rise building immersed in a rough-wall turbulent boundary layer. *J Wind Eng Ind Aerodyn* 2002;90:1151–62.
- [27] Kataoka H. Numerical simulations of a wind-induced vibrating square cylinder within turbulent boundary layer. *J Wind Eng Ind Aerodyn* 2008;96:1985–97.
- [28] Jiang G, Yoshie R, Shirasawa T, Jin X. Inflow turbulence generation for large eddy simulation in non-isothermal boundary layers. *J Wind Eng Ind Aerodyn* 2012;104–106:369–78.
- [29] Huang SH, Li QS, Xu SL. Numerical evaluation of wind effects on a tall steel building by CFD. *J Constr Steel Res* 2007;63:612–27.
- [30] Daniels SJ, Castro IP, Xie ZT. Peak loading and surface pressure fluctuations of a tall model building. *J Wind Eng Ind Aerodyn* 2013;120:19–28.
- [31] Fluent, Inc. The user guide of Fluent 14.0.0; 2011.
- [32] Tominaga Y, Mochida A, Yoshie R, Kataoka H, Nozu T, Yoshikawa M, Shirasawa T. AJ guidelines for practical applications of CFD to pedestrian wind environment around buildings. *J Wind Eng Ind Aerodyn* 2008;96:1749–61.
- [33] Raupach MR, Antonia RA, Rajagopalan S. Rough-wall turbulent boundary layers. *Appl Mech Rev* 1991;44(1):1–25.
- [34] Lettau HH. Note on aerodynamic roughness-parameter estimation on the basis of roughness element description. *J Appl Meteorol* 1969;8:828–32.
- [35] Wooding RA, Bradley EF, Marshall JK. Drag due to regular arrays of roughness elements of varying geometry. *Bound-Layer Meteor* 1973;5:285–308.
- [36] Liu G, Xuan J, Park S. A new method to calculate wind profile parameters of the wind tunnel boundary layer. *J Wind Eng Ind Aerodyn* 2003;91(9):1155–62.
- [37] Melbourne WH. Comparison of measurements of the CAARC standard tall building model in simulated model wind flows. *J Wind Eng Ind Aerodyn* 1980;6:78–88.
- [38] Obasaju ED. Measurement of forces and base overturning moments on the CAARC tall building model in a simulated atmospheric boundary layer. *J Wind Eng Ind Aerodyn* 1992;40:103–26.

- [39] Huang P, Luo P, Gu M. Pressure and forces measurements on CAARC standard Tall building in wind tunnel of Tong Ji University. In: Proceedings of the 12th national wind engineering conference of China; 2005. p. 240–4.
- [40] Franke J, Hellsten A, Schluzen H, Carissimo B. Best practice guideline for the CFD simulation of flows in the urban environment. Brussels: COST Office; 2007.
- [41] Chorin AJ. Numerical solution of Navier–Stokes equations. *Math Comput* 1968;22:745–62.
- [42] Iannuzzi A, Spinelli P. Artificial wind generation and structural response. *J Struct Div (ASCE)* 1987;113(12):2382–98.
- [43] Lumley JL, Panofsky HA. The structure of atmospheric turbulence. New York: Wiley-Interscience; 1964.
- [44] Li QS, Melbourne W. An experimental investigation of the effects of free-stream turbulence on streamwise surface pressures in separated and reattaching flows. *J Wind Eng Ind Aerodyn* 1995;54:313–23.
- [45] Goliger A, Milford R. Sensitivity of the CAARC standard building model to geometric scale and turbulence. *J Wind Eng Ind Aerodyn* 1988;31:105–23.
- [46] Martinuzzi R. Experimentelle untersuchung der umströmung wandgebundener, rechteckiger, prismatischer Hindernisse. Dissertation, University Erlangen-Nürnberg; 1992.
- [47] Davies ME, Quincey VG, Tindall SJ. The near-wake of a tall building block in uniform and turbulent flows. In: Cermak JE, editor. *Wind eng*. Oxford: Pergamon Press; 1980.